Research Article Vol. 32, No. 4 / 12 Feb 2024 / Optics Express 5932
Optics EXPRESS

Dissipative coupling in a Bragg-grating-coupled single resonator with Fano resonance for anti-PT-symmetric gyroscopes

MARTINO DE CARLO,[1,*] FRANCESCO DE LEONARDIS,[1] FRANCESCO DELL'OLIO,[1] YUNHONG DING,[2] AND VITTORIO M. N. PASSARO[1]

[1]*Department of Electrical and Information Engineering, Politecnico di Bari, Via Orabona 4, Bari 70126, Italy*
[2]*Department of Electrical and Photonics Engineering, Technical University of Denmark (DTU), 2800 Kgs. Lyngby, Denmark*
[*]*martino.decarlo@poliba.it*

Abstract: Anti-parity-time-symmetric Hamiltonians show an enhanced sensitivity to external perturbations that can be used for high-performance angular velocity sensing. Dissipative coupling is a valuable way for realizing anti-PT-symmetric Hamiltonians with optical resonators and is usually obtained by means of auxiliary waveguides. Here, we model and experimentally show the dissipative coupling between two counterpropagating modes of a single resonator, by means of a Bragg-grating placed in the feeding bus. The proposed solution enables the possibility of accurately designing the dissipative coupling strength in integrated non-Hermitian gyroscopes, thus providing high flexibility in the design of the proposed sensor. Moreover, we theoretically and experimentally demonstrate that the dissipative coupling between two counterpropagating modes of the same resonant cavity can give rise to an asymmetric Fano resonance.

1. Introduction

Non-Hermitian (NH) photonics has attracted a lot of attention in the recent research, because of various properties of exceptional points (EPs). The major interest for NH photonics is related to sensing [1] and non-reciprocal switching [2,3]. The attention for sensing applications has been mainly oriented to angular velocity sensing [4–8] and particle sensing [9–15] applications. Indeed, the existence of an EP leads to the high sensitivity of eigenfrequency response to external perturbations applied to the system [1], that can be exploited in some sensing schemes. In order to realize a non-Hermitian Hamiltonian, some specific conditions should be verified: a parity-time (PT)-symmetric Hamiltonian should commute with the PT operator, whereas an anti-PT-symmetric Hamiltonian should satisfy the anticommutation relation with the PT operator [1].

Two directly coupled resonators with the same isolated resonances and balanced loss and gain can realize a PT-symmetric Hamiltonian and exhibit an EP [1]. In the same way two dissipatively coupled resonators with different isolated resonances can realize an anti-PT-symmetric Hamiltonian and show an EP [16]. The dissipative coupling in anti-PT-symmetric systems has been obtained in resonant optical systems by means of a tapered coupling fiber [6], auxiliary external waveguides [7,8,16] or an auxiliary dissipative resonator [16].

In this work we realize the dissipative coupling between two counterpropagating modes of a single integrated optical resonator by means of a Bragg grating placed in the feeding bus to propose an integrated non-Hermitian gyroscope. Moreover, we theoretically and experimentally demonstrate that this dissipative coupling can show a Fano-like asymmetric resonant line shape (in agreement with the work recently published in [17]): Fano resonance is a type of resonant

#510617 https://doi.org/10.1364/OE.510617
Journal © 2024 Received 31 Oct 2023; revised 14 Dec 2023; accepted 24 Jan 2024; published 5 Feb 2024

Optics EXPRESS

scattering phenomenon [18] giving rise to a generally asymmetric line-shape and representing an attractive solution for slow light [19,20], switching [21,22,23] and high performance sensing [24,25].

The proposed dissipative coupling mechanism is proposed here for an integrated non-Hermitian optical gyroscope. The same concept can be extended to particle sensing, absorption, and refractive index sensing [1].

2. Modelling

Let's consider a single optical resonator, supporting only two counterpropagating optical modes. The dynamic equations for the amplitude vector $\boldsymbol{a} = [a_1, a_2]^T$, (where a_1 and a_2 are the amplitudes of the counterpropagating modes, normalized such that their squared norm represent the energy stored in the corresponding mode), can be written as [26]:

$$\frac{d\boldsymbol{a}}{dt} = (jW - \Gamma)\boldsymbol{a} + D^T \boldsymbol{s_{in}} \tag{1}$$

$$\boldsymbol{s_{out}} = C\boldsymbol{s_{in}} + D\boldsymbol{a} \tag{2}$$

where $\boldsymbol{s_{in}} = [s_{in,1}, s_{in,2}]^{\mathrm{T}}$ is the input vector, $\boldsymbol{s_{out}} = [s_{out,1}, s_{out,2}]^{\mathrm{T}}$ is the output vector, and W and Γ are 2×2 Hermitian matrices, representing the resonant frequencies and the decay/coupling for the supported modes respectively:

$$W = \begin{bmatrix} \omega_1 & 0 \\ 0 & \omega_2 \end{bmatrix}, \tag{3}$$

$$\Gamma = \begin{bmatrix} \Gamma_{11} & \Gamma_{12} \\ \Gamma_{21} & \Gamma_{22} \end{bmatrix}. \tag{4}$$

The resonant modes get excited by the incoming waves (modelled with the input vector $\boldsymbol{s_{in}}$) and then couple with the outgoing waves (modelled with the output vector $\boldsymbol{s_{out}}$) at the output ports according to the coupling matrix D:

$$D = \begin{bmatrix} D_{11} & D_{12} \\ D_{21} & D_{22} \end{bmatrix}. \tag{5}$$

For a lossless and reciprocal coupler, the matrix C needs to be unitary and symmetric. Here we express C in a generalized way using the two parameters, ϕ and θ:

$$C = e^{j\phi} \begin{bmatrix} \sin\theta & j\cos\theta \\ j\cos\theta & \sin\theta \end{bmatrix}. \tag{6}$$

The scattering matrix C describes the direct pathway through which the incoming and outcoming waves can couple [27].

The following relations hold between the defined matrices [26]:

$$D^+ D = 2\Gamma \tag{7}$$

$$CD^* = -D \tag{8}$$

where the $^+$ represents the Hermitian transposed operator, and * designates the conjugate complex.

Optics EXPRESS

In the following section we will demonstrate the possibility of realizing dissipative coupling between the counterpropagating resonant modes of a single resonator, by means of a Bragg grating placed in the feeding bus. To show this we analyze a Bragg-grating-coupled single resonator, defined as "configuration A" and depicted in Fig. 1(a). Such a coupling method is conceptually different from the direct coupling, occurring when the Bragg grating is placed inside the resonator (configuration B, shown in Fig. 1(b)). The comparison between the two configurations will be clear in the following sections.

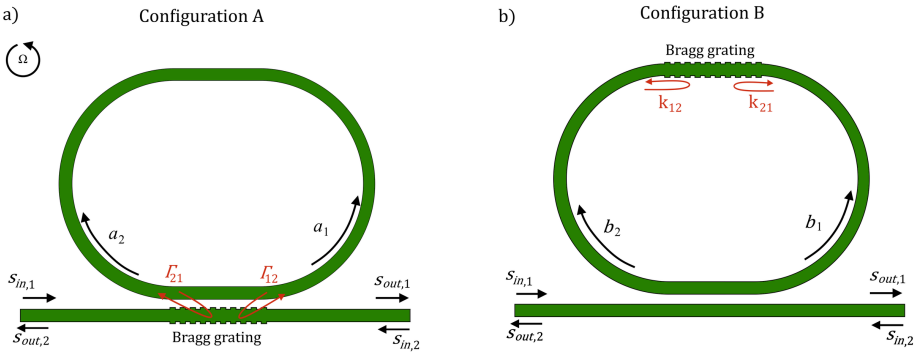

Fig. 1. Schematic representation of the two configurations analyzed in this work: (a) configuration A, realized with a racetrack resonator with a Bragg grating placed in the feeding bus in a centered position with respect to the racetrack resonator; (b) configuration B realized with a racetrack resonator with a Bragg grating inside the resonator itself.

Despite the focus of this work is on fully integrated sensors, the conclusions can be extended also to microtoroids in Silica, externally coupled to Fiber Bragg Gratings (FBGs) [28].

It is worth noting that in our modelling the backscattering inside the resonator arising from the nonidealities during propagation has not been taken into account, because it can be verified to be negligible with respect to the backscattering due to the Bragg gratings in both configurations.

2.1. Bragg-grating-coupled single resonator

In the case of a Bragg-grating coupled resonator (Fig. 1(a)), there is no direct coupling effect between the counterpropagating modes inside the resonator. Starting from Eq. (1) the coupled equations result to be [26] (with a_1 the counterclockwise mode and a_2 the clockwise mode, $s_{in,1}$ the excitation signal, and $s_{in,2} = 0$):

$$\frac{da_1}{dt} = (j\omega_1 a_1 - \Gamma_{11} a_1 - \Gamma_{12} a_2) + D_{11} s_{in,1} \tag{9}$$

$$\frac{da_2}{dt} = (j\omega_2 a_2 - \Gamma_{22} a_2 - \Gamma_{21} a_1) + D_{12} s_{in,1}. \tag{10}$$

Because of the presence of the Bragg grating in the feeding bus, all the terms of matrix D can be different from zero. Due to the symmetry of the architecture, $D_{12} = D_{21}$. If this happens, by using the Eqs. (7) and (8), the parameters Γ_{12} and Γ_{21} are found to be non-zero and real. Moreover, due to the symmetric architecture, $\Gamma_{12} = \Gamma_{21}$. They represent the dissipative coupling between a_2 and a_1 (and vice versa), due to the presence of the Bragg-grating in the feeding bus. In other words, the dissipative coupling terms (Γ_{12} and Γ_{21}) model the indirect coupling between the counterpropagating modes a_1 and a_2 (see Fig. 1(a)). In the absence of the grating (as in the configuration B) $\Gamma_{12} = \Gamma_{21} = 0$. In the presence of the grating, $\Gamma_{12} \neq 0$ and $\Gamma_{21} \neq 0$. In particular, the term ${\Gamma_{12}}^2$ (${\Gamma_{21}}^2$) is proportional to the power fraction of the circulating power in the resonator that indirectly couples from the mode a_2 (a_1) into the mode a_1 (a_2) [29].

Optics EXPRESS

The elements of the matrices Γ, D and C depend on the physical parameters of the Bragg grating. Moreover, the spectral feature of the Bragg grating response is assumed to be much broader than the spectral feature of the system modelled in (9) and (10), so the elements of the matrices Γ, D and C do not depend on wavelength.

Using Eqs. (9) and (10), it is possible to obtain the solution for a_1 and a_2, in the angular frequency (ω) domain, as:

$$a_1 = \frac{-\Gamma_{12}D_{12} + (j\omega - j\omega_2 + \Gamma_{22})D_{11}}{[(j\omega - j\omega_1 + \Gamma_{11})(j\omega - j\omega_2 + \Gamma_{22}) - \Gamma_{12}^2]} s_{in,1} \tag{11}$$

$$a_2 = \frac{-\Gamma_{21}D_{11} + (j\omega - j\omega_1 + \Gamma_{11})D_{12}}{[(j\omega - j\omega_2 + \Gamma_{22})(j\omega - j\omega_1 + \Gamma_{11}) - \Gamma_{12}^2]} s_{in,1} \tag{12}$$

and for the output signal at the output port as:

$$s_{out,1} = C_{11}s_{in,1} + D_{11}a_1 + D_{12}a_2. \tag{13}$$

In this configuration (A), θ and ϕ (see Eq. (6)) depend on the grating; in the absence of the grating, no reflections could happen in the direct pathway, implying $\cos(\theta) = 0$ (e.g., $\theta = \pi/2$). For a fully reflective Bragg grating, $|\cos(\theta)|=1$ (e.g., $\theta = 0$, there is not any direct pathway from $s_{in,1}$ to $s_{out,1}$, but $s_{in,1}$ is still coupled to $s_{out,1}$ by means of the resonant modes). The transmission spectra of this configuration are shown in Figs. 2(a), 2(b), 2(c) and 2(d) for four different values of the parameter θ, with $D_{11} = D_{22} = 2{\cdot}10^5$ (rad/s)$^{1/2}$ (being $\omega_0 = (\omega_1 + \omega_2)/2$) and with additional propagation loss $\Gamma_{ADD} = 10^9$ rad/s (added to the main diagonal elements of the matrix Γ). The other parameters are calculated using Eqs. (7) and (8). The transmission spectra are shown in the absence of perturbation (ω_1=ω_2, forced by design), so all the spectra shown in Fig. 2 are in the unbroken anti-PT-symmetric phase. In Figs. 2(a), 2(b) and 2(c), different values of ϕ are simulated. It is immediately shown that both asymmetric Fano resonant line shapes (Figs. 2(b) and 2(c)) and electromagnetic induced transparency (EIT) (Fig. 2(a)) can be induced. In particular EIT occurs when $|\cos(\theta)|=1$ (e.g., $\theta = 0$, corresponding to a fully reflective Bragg grating). In the absence of the grating (e.g., $\theta = \pi/2$ and $D_{12} = D_{21} = 0$, and $\phi = \pi$ is forced by Eq. (8)) (Fig. 2(d)) the spectrum corresponds to the one of a classical all-pass ring resonator. Asymmetric line shapes appear for intermediate values of $|\cos(\theta)|$ (Fig. 2(b) and 2(c)).

With coupled equations similar to (9) and (10), in [30] it has been demonstrated that it is possible to show a Fano-like resonant line shapes in a single ring resonator supporting two copropagating optical modes with $\omega_1 \neq \omega_2$. In our case, the condition $\omega_1 = \omega_2$ is forced by design (same TE transverse mode propagating in opposite directions) when the system is at rest (no angular rotation). Nevertheless, we have shown that is possible to exhibit Fano-like resonant line shapes even with $\omega_1 = \omega_2$, by properly designing the elements of matrix D.

Furthermore, the eigenfrequencies ($\omega_{A1,2}$) of the system are found to be:

$$\omega_{A_{1,2}} = \frac{\omega_1 + \omega_2}{2} + j\frac{\Gamma_{11} + \Gamma_{22}}{2} \pm \frac{1}{2}\sqrt{-(j(\omega_1 - \omega_2) + (\Gamma_{22} - \Gamma_{11}))^2 - 4\Gamma_{12}^2} \tag{14}$$

An exceptional point (EP) arises for:

$$(j(\omega_1 - \omega_2) + (\Gamma_{22} - \Gamma_{11}))^2 = -4\Gamma_{12}^2 \tag{15}$$

So, an EP is achievable only for $\Gamma_{22} = \Gamma_{11}$ and $\omega_1 \neq \omega_2$, such that:

$$\omega_1 - \omega_2 = (\omega_1 - \omega_2)_{EP} = \pm 2|\Gamma_{12}|. \tag{16}$$

If the system is set to work at the EP and a perturbation is applied to $\omega_1 - \omega_2$, the eigenfrequency splitting shows a highly sensitive dependence on the perturbation.

Optics EXPRESS

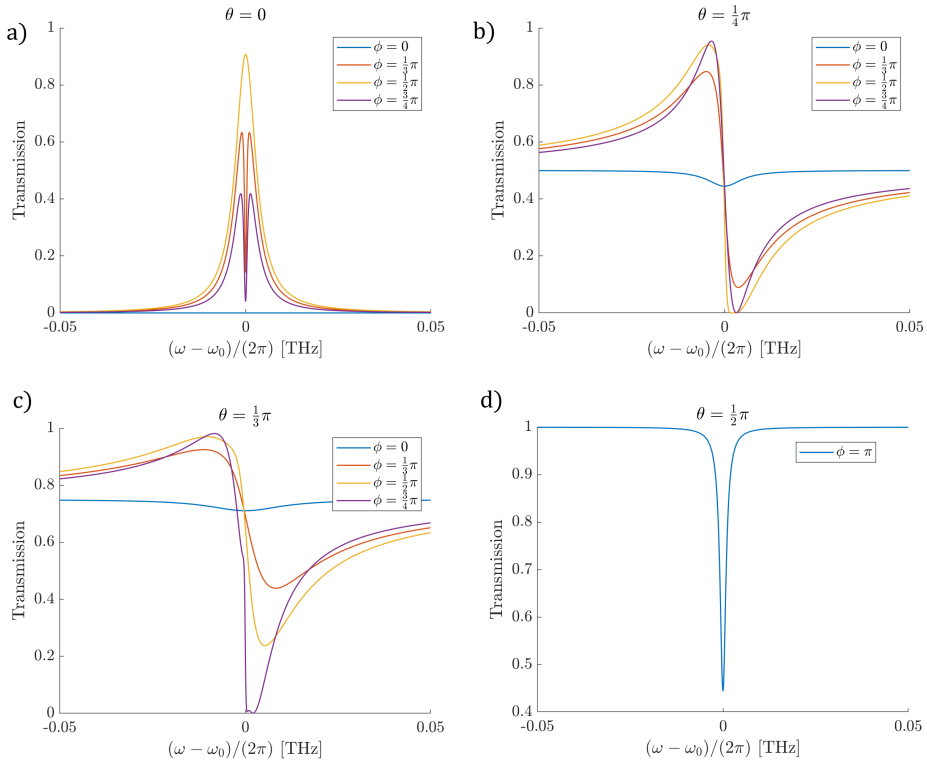

Fig. 2. Simulation results: plot of the simulated transmission spectrum $|s_{out,1}/s_{in,1}|^2$ as a function of the normalized frequency detuning for the configuration A, for different values of θ, and with $D_{11} = D_{22} = 2{\cdot}10^5$ (rad/s)$^{1/2}$ and with additional propagation loss $\Gamma_{ADD} = 10^9$ rad/s. In (a), (b) and (c), different values of parameter ϕ are simulated.

2.1.1. Anti-PT-symmetric gyroscope

An integrated optical gyroscope can be immediately realized with the configuration A, to sense the Sagnac-induced perturbation, $\omega_1 - \omega_2 \propto \Omega$ [7], being Ω the rotational speed of the device around an axis perpendicular to the surface of the device, as in Fig. 1(a). Its maximum sensitivity would be around a non-zero value of Ω [6]. However, in most of the applications where optical gyroscopes are used, high sensitivity is required for low angular velocities. So, in order to realize an integrated non-Hermitian optical gyroscope with improved performance using the proposed configuration A (Fig. 1(a)), two possible solutions can be implemented:

- either spinning the resonator at a known velocity in order to meet Eq. (16) [12];
- or inducing a non-reciprocal phase shift between the two counterpropagating modes inside the ring resonator, again to meet Eq. (16).

In both cases, the eigenfrequency splitting of the proposed gyroscope is found to be:

$$\Delta\omega_{APT,\Omega} \approx 4\sqrt{|\Gamma_{12}|\frac{2\pi A\Omega}{\lambda P n_{\text{eff}}}}, \tag{17}$$

where A is the area enclosed by the resonator, P is the perimeter of the resonator, n_{eff} is the effective index of the transverse mode in the resonator.

Optics EXPRESS

It can be noticed that the eigenfrequency splitting depends on the square root of the angular velocity, thus guaranteeing high sensitivity of the gyroscope for small angular velocities. Since Γ_{12} is related to the reflectance of the Bragg grating, the proposed configuration provides high flexibility in the sensor design. The sensitivity of the gyroscope is proportional to the square root of the dissipative coupling term, which in turn depends on the Bragg grating. Figure 3 shows the eigenfrequency splitting as a function of the angular velocity Ω, with $A = 13710\ \mu m^2$, $P = 417\ \mu m$ (same values used in the experimental configurations), at λ=1.55 µm and with $n_{eff} = 2.39$.

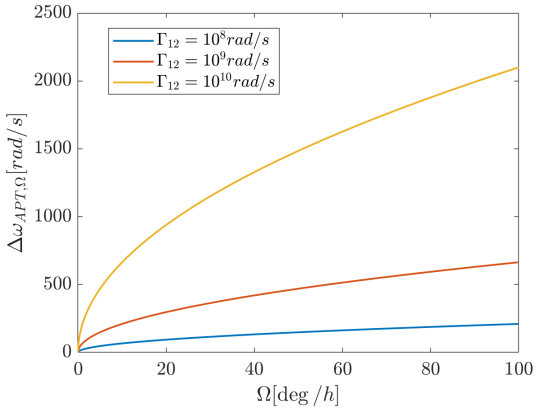

Fig. 3. Eigenfrequency splitting of the anti-PT-symmetric gyroscope as a function of the angular velocity, for different values of the dissipative coupling term, Γ_{12}.

2.1.2. Other sensing applications

It is worth noting that by using one of the proposed solutions (non-reciprocal phase shift or externally induced rotation) to set the system at the EP, other sensing applications can be implemented with the configuration A:

- particle sensing: the presence of a particle interacting with the counterpropagating modes inside the resonator also induces a direct coupling strength (jk_{12}), which the eigenfrequency are highly sensitive to. In this case the eigenfrequency splitting would be equal to (assuming $k_{12} = k_{21}$) [12]:

$$\Delta\omega_{APT,P} \approx 2\sqrt{2j\Gamma_{12}k_{12}} \tag{18}$$

- Bragg-grating-based refractive-index sensing: the Bragg grating represents a sensing element that can be used for sensing (i.e., refractive-index-based sensing). In fact, by defining a perturbation applied to the Bragg grating (such that the perturbed dissipative coupling strength is equal to $\Gamma_{12} - \Delta\kappa_B$), the eigenfrequency splitting is found to be:

$$\Delta\omega_{APT,B} \approx 2\sqrt{2\Gamma_{12}\Delta\kappa_B} \tag{19}$$

The square root dependence on the perturbation $\Delta\kappa_B$ implies an increased sensitivity for the Bragg grating sensor. Also in these two cases, the sensitivity of the sensor is proportional to the square root of Γ_{12}.

2.2. Bragg-grating inside the resonator

The dissipative coupling shown in the previous section is conceptually different from the direct coupling occurring between two counterpropagating modes in a resonator, in the presence

Optics EXPRESS

of backscattering between counterpropagating modes. In order to underline the difference between the two coupling mechanisms, we also model the waveguide-coupled resonator with Bragg-grating inside the resonator (see Fig. 1(b)). We would like to emphasize that the aim of the modelling and experimental verification of the configuration B is to highlight the differences occurring in placing the Bragg grating inside (direct coupling) or outside (dissipative coupling) the resonator.

In this case it is necessary to include the terms jk_{12} and jk_{21} in the coupled mode theory to take into account the direct coupling strengths between the two counterpropagating modes inside the resonator [26]. In this case it is immediate to note the cross-diagonal elements of the matrix D are null and, consequently, the cross-diagonal elements of matrix Γ are null. The symmetry of the architecture further suggests $D_{11} = D_{22}$ and $k_{12} = k_{21}$. The temporal coupled mode equations can be now written in terms of the amplitude vector $\boldsymbol{b} = [b_1, b_2]^{\mathrm{T}}$ (with b_1 the counterclockwise mode and b_2 the clockwise mode, $s_{in,1}$ the excitation signal, and $s_{in,2} = 0$):

$$\frac{db_1}{dt} = (j\omega_1 b_1 - \Gamma_{11} b_1 + jk_{12} b_2) + D_{11} s_{in,1} \tag{20}$$

$$\frac{db_2}{dt} = (j\omega_2 b_2 - \Gamma_{22} b_2 + jk_{21} b_1) \tag{21}$$

So, it is possible to obtain the expression for b_1 and b_2:

$$b_1 = \frac{(-\Gamma_{12} + jk_{12})D_{12} + (j\omega - j\omega_2 + \Gamma_{22})D_{11}}{[(j\omega - j\omega_1 + \Gamma_{11})(j\omega - j\omega_2 + \Gamma_{22}) - (\Gamma_{12} - jk_{12})(\Gamma_{21} - jk_{12})]} s_{in,1} \tag{22}$$

$$b_2 = \frac{-(\Gamma_{21} - jk_{21})D_{11} + (j\omega - j\omega_1 + \Gamma_{11})D_{12}}{[(j\omega - j\omega_2 + \Gamma_{22})(j\omega - j\omega_1 + \Gamma_{11}) - (\Gamma_{12} - jk_{12})(\Gamma_{21} - jk_{12})]} s_{in,1} \tag{23}$$

Thus, we obtain:

$$s_{out,1} = C_{11} s_{in,1} + D_{11} b_1 \tag{24}$$

The simulated transmission spectrum of this configuration is shown in Fig. 4, for different values of k_{12}.

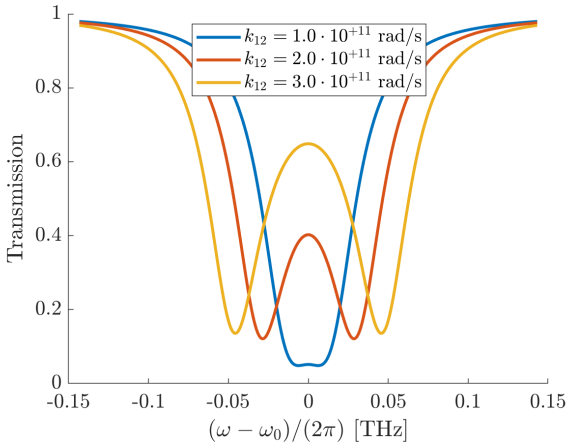

Fig. 4. Simulation results: plot of the simulated transmission spectrum $|s_{out,1}/s_{in,1}|^2$ as a function of the normalized frequency detuning for the configuration B, for different values of the direct coupling strength k_{12}.

Optics EXPRESS

Furthermore, the eigenfrequencies of the modelled system are obtained as:

$$\omega_{B1,2} = \frac{\omega_1 + \omega_2}{2} + j\frac{\Gamma_{11} + \Gamma_{22}}{2} \pm \frac{1}{2}\sqrt{-(j(\omega_1 - \omega_2) + (\Gamma_{22} - \Gamma_{11}))^2 + 4k_{12}k_{21}} \quad (25)$$

An exceptional point is obtained for:

$$(j(\omega_1 - \omega_2) + (\Gamma_{22} - \Gamma_{11}))^2 = 4k_{12}k_{21} \quad (26)$$

So, this can only be achieved with $\omega_1 = \omega_2$ (forced by design) and non-reciprocal loss/gain ($\Gamma_{22} \neq \Gamma_{11}$). Such an approach can be used to realize a non-Hermitian Hamiltonian for a high-performance gyroscope [31].

3. Experimental results

Both the proposed configurations, shown in Figs. 1(a) and 1(b), have been designed, realized and optically characterized. The devices were fabricated with silicon-on-insulator technology, using 450 nm × 250 nm strip waveguides (by e-beam lithography). The racetrack resonator has been designed with a curvature radius of 60 µm and the straight sections 20 µm long. The Bragg grating has been designed to be placed in two different positions, in the feeding bus for the configuration A (Fig. 5(a)), and inside the resonator for the configuration B (Fig. 5(b)). In both cases, the Bragg grating is designed with 25-nm wide teeth on each side, 42 periods, 50% duty cycle and 310 nm period, corresponding to a simulated Bragg wavelength of 1530 nm and maximum power reflection of 55% (when only the Bragg grating is simulated). Moreover, we verified with numerical simulations of the coupling region of the configuration A, that ${\Gamma_{12}}^2$ increases while increasing the number of grating periods from 0 to 60. In the configuration A (Fig. 5(a)), the resonator-bus waveguide gap is 250 nm, while in the configuration B (Fig. 5(b)), the bus-resonator gap is 300 nm.

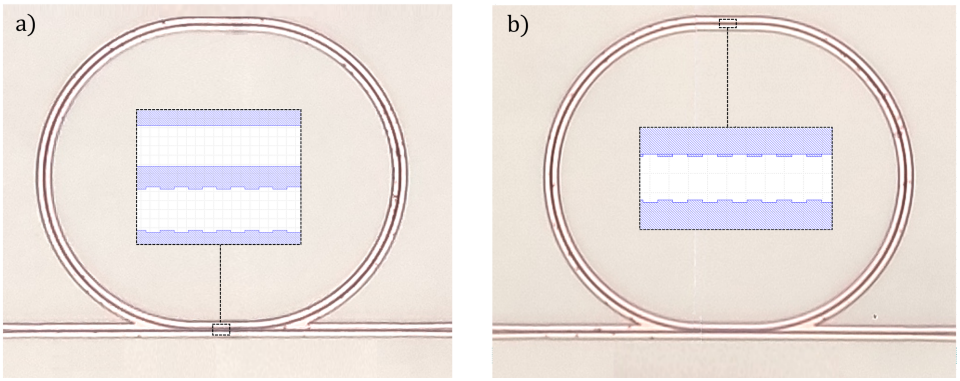

Fig. 5. Two microscope pictures of the devices realized according to configurations A (a) and B (b). The insets in each picture show the detail of the Bragg grating in each of the designs according to the layout that has been used for the fabrication.

Figures 5(a) and 5(b) show two microscope pictures of the devices realized according to configurations A and B, respectively. The insets in each picture show the detail of the relevant Bragg gratings.

The measurements have been taken by sweeping the wavelength of a tunable laser source.

Figure 6(a) shows the measured spectrum of the device for configuration A. The measurements are taken at rest, $\omega_1 = \omega_2$, thus implying that the anti-PT-symmetric system is in the unbroken phase. In particular, it is possible to observe the Fano-like asymmetric line shapes of the

Optics EXPRESS

resonances, as expected from Figs. 2(b) and 2(c). Figure 6(b) shows one measured asymmetric line shape resonance and its fitted curve, using the analytical expression of Eq. (13) together with (11)-(12). Table 1 shows the fitting of independent parameters, giving high agreement between theory and experiments ($R^2 = 0.9964$). The remaining dependent parameters are obtained using Eqs. (6), (7) and (8) (e.g., $\Gamma_{12} = 3.5545 \cdot 10^{10}$ rad/s).

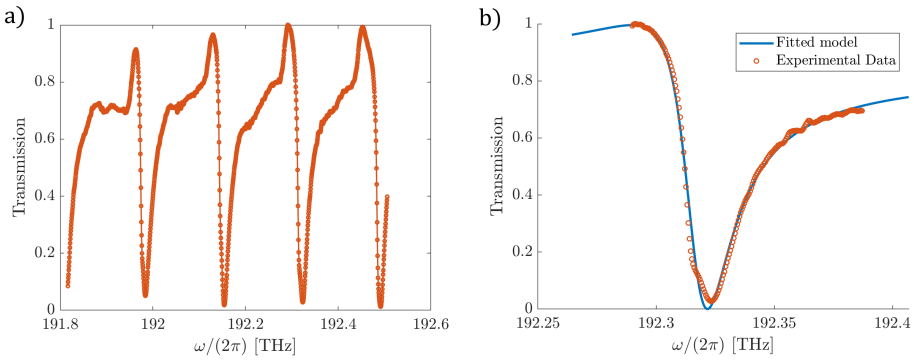

Fig. 6. Experimental results: (a) measured transmission spectrum of the fabricated device in configuration A; (b) zoom on a resonance of the transmission spectrum in configuration A and fit with the proposed analytical model.

Table 1. Fitted parameters in configurations A and B

Symbol	Configuration A	Configuration B
D11 (= D22)	$1.8849 \cdot 10^5$ (rad/s)$^{1/2}$	$3.4099 \cdot 10^5$ (rad/s)$^{1/2}$
ϕ	2.7354	0
θ	1.1648	3/2 π
ω_0	$1.20836 \cdot 10^{15}$ rad/s	$1.206175 \cdot 10^{15}$ rad/s
Γ_{ADD}	$1.0497 \cdot 10^9$ rad/s	$2.7160 \cdot 10^{10}$ rad/s
k_{12}	0	$9.7884 \cdot 10^{10}$ rad/s
R^2	0.9933	0.9918

Figure 7(a) shows the experimental spectrum for the configuration B. It is possible to see that each resonance shows two dips. This is in agreement with the theoretical results and the simulations shown in Fig. 4, as expected. In Fig. 7(b) the fit of one resonance line shape of the measured spectrum is sketched according to our modelling, by using Eq. (24) together with Eqs. (22) and (23). The obtained fitting independent parameters are summarized in Table 1. The good agreement between the model and the experimental results is proved by the value of R^2 of 0.9917.

The experimental data of both configurations, fitted by the corresponding models, highlight the different effects of dissipative and direct coupling on the output spectrum; in particular the good agreement between theory and experiment confirms the validity of the proposed model for the two configurations with the dissipative coupling and the direct one. The solution implementing a Bragg grating in the feeding bus (configuration A) suggests a valuable possibility to realize the dissipative coupling in a fully integrated anti-PT-symmetric gyroscope, with good flexibility in the design of the dissipative coupling strength.

Finally, we would like to highlight that the proposed structure shows an important advantage with respect to previously proposed architectures for anti-PT-symmetric gyroscopes [7,8], related to the robustness to parameter fluctuations. Using a single resonator rather than two drastically

Optics EXPRESS

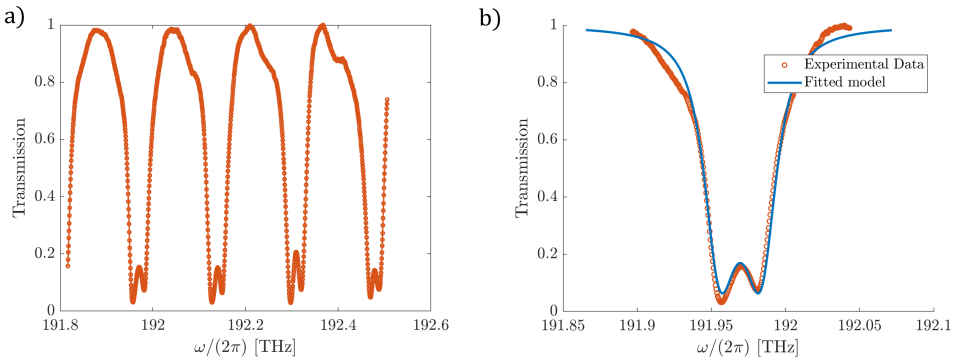

Fig. 7. Experimental results: (a) measured transmission spectrum of the fabricated device in configuration B; (b) zoom on a resonance of the transmission spectrum in configuration B and fit with the proposed analytical model.

reduces the influence of differential perturbations on counterpropagating modes. Moreover, dealing with noise (widely debated in the context of non-Hermitian photonics [32–36]), it has been recently demonstrated that an enhanced signal-to-noise ratio can be achieved with respect to classical sensing architectures, when working close to EPs below the lasing threshold [37,38]. The enhancement of the signal-to-noise ratio also occurs in the architecture proposed in this manuscript for an anti-PT-symmetric gyroscope (configuration A).

4. Conclusions

We have modelled and experimentally measured the transmission spectrum of a Bragg-grating-coupled optical resonator, able to realize an anti-parity-time symmetric optical gyroscope.

The highly accurate agreement between the theoretical modelling and the measurements suggests the real possibility of realizing an integrated non-Hermitian optical gyroscope, by means of dissipative coupling, enabled by a Bragg grating. This provides a useful way to realize the desired the dissipative coupling for the sensitivity of the anti-parity-time-symmetric gyroscope.

Finally, the presented device has also theoretically and experimentally shown a typical asymmetric Fano-like resonant line shape, that could be further useful for other sensing or switching applications.

Funding. Fondo Sociale Europeo REACT EU - Programma Operativo Nazionale Ricerca e Innovazione 2014–2020 by Ministero dell'Università e della Ricerca (D95F21002140006).

Acknowledgments. Martino De Carlo has been supported by Fondo Sociale Europeo REACT EU - Programma Operativo Nazionale Ricerca e Innovazione 2014–2020 by Ministero dell'Università e della Ricerca (D95F21002140006).

Disclosures. The authors declare no conflicts of interest.

Data availability. Data underlying the results presented in this paper are not publicly available at this time but may be obtained from the authors upon reasonable request.

References

1. J. Wiersig, "Review of exceptional point-based sensors," Photonics Res. **8**(9), 1457 (2020).
2. X.-L. Zhang, T. Jiang, and C. T. Chan, "Dynamically encircling an exceptional point in anti-parity-time symmetric systems: asymmetric mode switching for symmetry-broken modes," Light: Sci. Appl. **8**(1), 88 (2019).
3. Y. Wei, H. Zhou, Y. Chen, *et al.*, "Anti-parity-time symmetry enabled on-chip chiral polarizer," Photonics Res. **10**(1), 76 (2022).
4. J. Ren, H. Hodaei, G. Harari, *et al.*, "Ultrasensitive micro-scale parity-time-symmetric ring laser gyroscope," Opt. Lett. **42**(8), 1556 (2017).
5. M. De Carlo, F. De Leonardis, and V. M. N. Passaro, "Design Rules of a Microscale PT-Symmetric Optical Gyroscope Using Group IV Platform," J. Lightwave Technol. **36**(16), 3261–3268 (2018).

Optics EXPRESS

6. Y.-H. Lai, Y.-K. Lu, M.-G. Suh, *et al.*, "Observation of the exceptional-point-enhanced Sagnac effect," Nature **576**(7785), 65–69 (2019).
7. M. De Carlo, F. De Leonardis, L. Lamberti, *et al.*, "High-sensitivity real-splitting anti-PT-symmetric microscale optical gyroscope," Opt. Lett. **44**(16), 3956 (2019).
8. M. De Carlo, F. De Leonardis, L. Lamberti, *et al.*, "Design of a resonator-bus-resonator anti-parity-time-symmetric integrated optical gyroscope," Opt. Lasers Eng. **153**, 106983 (2022).
9. J. Wiersig, "Enhancing the Sensitivity of Frequency and Energy Splitting Detection by Using Exceptional Points: Application to Microcavity Sensors for Single-Particle Detection," Phys. Rev. Lett. **112**(20), 203901 (2014).
10. W. Chen, Ş. Kaya Özdemir, G. Zhao, *et al.*, "Exceptional points enhance sensing in an optical microcavity," Nature **548**(7666), 192–196 (2017).
11. W. Li, H. Zhang, P. Han, *et al.*, "Real frequency splitting indirectly coupled anti-parity-time symmetric nanoparticle sensor," J. Appl. Phys. **128**(13), 1 (2020).
12. H. Zhang, R. Huang, S.-D. Zhang, *et al.*, "Breaking Anti-PT Symmetry by Spinning a Resonator," Nano Lett. **20**(10), 7594–7599 (2020).
13. W. Chen, J. Zhang, B. Peng, *et al.*, "Parity-time-symmetric whispering-gallery mode nanoparticle sensor [Invited]," Photonics Res. **6**(5), A23 (2018).
14. S. Jiang, Z. Xiao, W. Li, *et al.*, "Enhanced nanoparticle sensing by mode intensity in a non-reciprocally coupled microcavity," J. Appl. Phys. **131**(10), 1 (2022).
15. H. Hodaei, A. U. Hassan, S. Wittek, *et al.*, "Enhanced sensitivity at higher-order exceptional points," Nature **548**(7666), 187–191 (2017).
16. F. Yang, Y.-C. Liu, and L. You, "Anti- PT symmetry in dissipatively coupled optical systems," Phys. Rev. A **96**(5), 053845 (2017).
17. T. Wang, "Generalized temporal coupled-mode theory for a P T-symmetric optical resonator and Fano resonance in a P T-symmetric photonic heterostructure," Opt. Express **30**(21), 37980 (2022).
18. M. F. Limonov, M. V. Rybin, A. N. Poddubny, *et al.*, "Fano resonances in photonics," Nat. Photonics **11**(9), 543–554 (2017).
19. B. Ruan, M. Li, C. Liu, *et al.*, "Slow-light effects based on the tunable Fano resonance in a Tamm state coupled graphene surface plasmon system," Phys. Chem. Chem. Phys. **25**(3), 1685–1689 (2023).
20. H.-J. Chen, "The fast–slow light transitions induced by Fano resonance in multiple nanomechanical resonators," Optics Laser Technol. **161**, 109242 (2023).
21. L. Stern, M. Grajower, and U. Levy, "Fano resonances and all-optical switching in a resonantly coupled plasmonic–atomic system," Nat. Commun. **5**(1), 4865 (2014).
22. D. Seo, J. K. Lee, and G. C. Park, "Active Fano resonance switch using dual-layer graphene in an embedded dielectric metasurface," Opt. Express **30**(12), 22247 (2022).
23. M. Amin, R. Ramzan, and O. Siddiqui, "Fano resonance based ultra high-contrast electromagnetic switch," Appl. Phys. Lett. **110**(18), 1 (2017).
24. K. P. Heeg, C. Ott, D. Schumacher, *et al.*, "Interferometric phase detection at x-ray energies via Fano resonance control," Phys. Rev. Lett. **114**(20), 207401 (2015).
25. N. S. King, L. Liu, X. Yang, *et al.*, "Fano Resonant Aluminum Nanoclusters for Plasmonic Colorimetric Sensing," ACS Nano **9**(11), 10628–10636 (2015).
26. Wonjoo Suh, Zheng Wang, and Shanhui Fan, "Temporal coupled-mode theory and the presence of non-orthogonal modes in lossless multimode cavities," IEEE J. Quantum Electron. **40**(10), 1511–1518 (2004).
27. S. Fan, W. Suh, and J. D. Joannopoulos, "Temporal coupled-mode theory for the Fano resonance in optical resonators," J. Opt. Soc. Am. A **20**(3), 569 (2003).
28. F. Anelli, A. Annunziato, M. Godfrey, *et al.*, "Effects of Curvature on Flexible Bragg Grating in Off-Axis Core: Theory and Experiment," J. Lightwave Technol. **41**(9), 2904–2910 (2023).
29. B. E. Little, S. T. Chu, H. A. Haus, *et al.*, "Microring resonator channel dropping filters," J. Lightwave Technol. **15**(6), 998–1005 (1997).
30. B.-B. Li, Y.-F. Xiao, C.-L. Zou, *et al.*, "Experimental observation of Fano resonance in a single whispering-gallery microresonator," Appl. Phys. Lett. **98**(2), 1 (2011).
31. M. P. Hokmabadi, A. Schumer, D. N. Christodoulides, *et al.*, "Non-Hermitian ring laser gyroscopes with enhanced Sagnac sensitivity," Nature **576**(7785), 70–74 (2019).
32. W. Langbein, "No exceptional precision of exceptional-point sensors," Phys. Rev. A **98**(2), 023805 (2018).
33. H. Wang, Y.-H. Lai, Z. Yuan, *et al.*, "Petermann-factor sensitivity limit near an exceptional point in a Brillouin ring laser gyroscope," Nat. Commun. **11**(1), 1610 (2020).
34. L. Horstman, N. Hsu, J. Hendrie, *et al.*, "Exceptional points and the ring laser gyroscope," Photonics Res. **8**(3), 252 (2020).
35. L. Horstman and J.-C. Diels, "Intracavity Measurement Sensitivity Enhancement without Runaway Noise," Sensors **21**(24), 8473 (2021).
36. D. D. Smith, H. Chang, E. Mikhailov, *et al.*, "Beyond the Petermann limit: Prospect of increasing sensor precision near exceptional points," Phys. Rev. A **106**(1), 013520 (2022).
37. R. Kononchuk, J. Cai, F. Ellis, *et al.*, "Exceptional-point-based accelerometers with enhanced signal-to-noise ratio," Nature **607**(7920), 697–702 (2022).
38. M. De Carlo, F. De Leonardis, and V. M. N. Passaro, "Anti-PT-symmetric optical gyroscope at the transmission peak degeneracy with enhanced signal-to-noise ratio," J. Lightwave Technol. **42**(2), 936–944 (2024).